

Soft Matter

Accepted Manuscript

This article can be cited before page numbers have been issued, to do this please use: L. Stricker, S. Charlton and E. Secchi, *Soft Matter*, 2026, DOI: 10.1039/D5SM01062D.



This is an Accepted Manuscript, which has been through the Royal Society of Chemistry peer review process and has been accepted for publication.

Accepted Manuscripts are published online shortly after acceptance, before technical editing, formatting and proof reading. Using this free service, authors can make their results available to the community, in citable form, before we publish the edited article. We will replace this Accepted Manuscript with the edited and formatted Advance Article as soon as it is available.

You can find more information about Accepted Manuscripts in the [Information for Authors](#).

Please note that technical editing may introduce minor changes to the text and/or graphics, which may alter content. The journal's standard [Terms & Conditions](#) and the [Ethical guidelines](#) still apply. In no event shall the Royal Society of Chemistry be held responsible for any errors or omissions in this Accepted Manuscript or any consequences arising from the use of any information it contains.

Cite this: DOI: 00.0000/xxxxxxxxxx

Multiscale reorganisation of colloidal aggregation by percolating bacterial networks

Laura Stricker^{*a†}, Samuel Charlton ^{*b†}, and Eleonora Secchi^{b†}Received Date
Accepted Date

DOI: 00.0000/xxxxxxxxxx

Self-assembly in colloidal suspensions emerges from the interplay of local ordering and constraints imposed by the surrounding medium. While motile bacteria are known to alter colloidal dynamics, the influence of non-motile species remains largely unexplored. Here, we study suspensions of colloids and non-motile *Comamonas denitrificans* sedimenting near the wall and forming percolating networks. Using multiscale structural descriptors, we show that bacteria enhance colloidal aggregation into branch-like clusters. In turn, colloids reinforce bacterial networks by extending their elastic backbone. The analysis of mid-range ordering reveals that, unlike purely colloidal suspensions where ordering propagates across 3–4 neighbour shells, bacterial scaffolds suppress this propagation beyond the first shell. These findings highlight how non-motile bacteria reshape colloidal self-assembly across scales, while providing a quantitative framework for studying complex particle–network interactions. This approach opens pathways to understanding analogous processes in natural systems, including those involving microplastic contaminants.

Bacterial sedimentation is central to geochemical cycling, contributing to pollutant sequestration and carbon storage in sediments¹. Across the terrestrial and marine environments, bacteria coexist with particulate matter, such as mineral grains, organic-rich soil aggregates, and particulate organic carbon^{2–4}. However, the dynamics of bacteria-particle interactions remain poorly understood. Most existing work has focused on motile species. Motile bacteria can hinder particle settling, drive the propagation of topological defects in dense colloidal mixtures, and are themselves accelerated when swimming in proximity to colloids^{5–9}. These phenomena are exploited in applications such as bacteria-driven mixing and interface stabilisation^{10–12}. In non-motile systems, studies have largely focused on monospecies suspensions where passive interactions such as depletion attraction and polymer bridging establish aggregation, and phenotypic traits such as filamentation control the topology and mechanics of the resulting networks¹³. Less understood is the effect of non-motile bacteria on the formation of colloidal aggregates and networks, as well as the influence of colloidal–bacterial interactions on the development and settling of bacterial flocs.

Here, we study mixed suspensions of colloids and non-motile *Comamonas denitrificans* bacteria with similar sedimentation velocities. We focus on how the percolating bacterial network af-

fects the near-wall layer colloidal structuring at different length scales; local (nearest neighbours), mid-range, and global (system-spanning) and how colloids in turn influence the bacterial network. Our analysis is based on two-dimensional projections of sedimented near-wall layer and focuses on relative structural differences between bacteria–colloid mixtures and colloids-only suspensions. Using a combination of structural analysis and multiscale metrics, we characterise the self-assembly mechanisms that emerge in such mixed suspensions. Though multiscale analysis has been previously proposed to study hierarchical clustering and network formation gelation in soft particulate systems^{14,15}, to the best of our knowledge, this approach has not yet been used to investigate bacterial suspensions. We interpret our results within the framework of self-assembly, which arises from the minimisation of free energy—either through internal energy reduction, associated with short-range ordering via ‘locally favoured structures’ (LFS)^{16,17}, or through entropy maximisation, which is conversely related to ordering at a larger scale^{18,19}. Geometric confinement strongly modulates colloidal clustering^{20–23}, and in our system, the near-wall bacterial network imposes such constraints. In our system, short-range ordering remains unaffected, but pronounced changes occur at the mid-range and global scales. We explore this decoupling between length scales using tools from information theory, specifically mutual information²⁴, and from graph theory, through clique identification methods²⁵. While previous studies have hinted at a connection between local entropy, which is related to mid-range ordering, and locally favoured structures²⁶, our analysis offers a broader, multiscale perspective.

* These authors contributed equally to the present work

^a Otto von Guericke University Magdeburg, Institute of Process Engineering, 39106 Magdeburg, Germany.^b ETH Zurich, Institute of Environmental Engineering, 8093, Zurich, Switzerland.

Corresponding authors: †laura.stricker@ovgu.de, †charlton@ifu.baug.ethz.ch, †secchi@ifu.baug.ethz.ch



1 Materials and methods

1.1 Experimental System

Experiments were conducted by preparing liquid mixtures of colloidal particles and *Comamonas denitrificans* (referred to as 'mixed suspensions') and imaging their behaviour via optical microscopy. These were compared against two control conditions: suspensions containing only colloids ('colloids-only') and suspensions containing only bacteria ('bacteria-only'). All suspensions were loaded into rectangular glass capillaries ($0.25 \times 10 \times 40$ mm³; Vitrocom, USA), with approximately ≈ 300 μ L of sample per experiment. The ends of the capillaries were sealed with Vaseline to prevent evaporation, and the vessels were immediately transferred to the microscope stage. Structures formed at the bottom of the chamber were analysed after 140 minutes, once sedimentation was complete.

1.2 Bacterial culture

We perform the experiments using *Comamonas denitrificans* 123 (ATCC 700936), a rod-shaped, Gram-negative bacterium, cultured under conditions optimised to produce a narrow cell length distribution, with an average length of 4.16 μ m and a standard deviation of 1.25 μ m (see Fig. 2.b). Glycerol cryostocks were routinely revived by inoculating 5 mL of Tryptic Soy Broth (TSB; Sigma-Aldrich) and incubating overnight at 30° with shaking at 180 rpm in 50 mL Falcon centrifuge tubes. The following day, subcultures were prepared by diluting the overnight culture 1:100 (v/v) into fresh 5 mL TSB and incubating for 6 h at 30° under the same shaking conditions, until cultures reached an optical density (OD_{600}) of 1.0. Bacterial cell suspensions were aliquoted into 1.5 mL centrifuge tubes and washed three times with fresh TSB by centrifugation at 2700 rcf for 90 seconds. After the final wash, the cell pellets were resuspended in TSB containing the colloidal suspension for downstream assays.

1.3 Colloidal Particles Selection and Preparation

For the mixed and the colloids-only suspensions, we use Fluor-Red polystyrene colloids (2.5% w/v) with a diameter of 3.0 μ m (microParticles GmbH, Germany), suspended in conditioned bacterial culture medium. The conditioned medium was obtained by filtering a bacterial culture $OD_{600} = 1$ through a 0.2 μ m filter (Filtropur S 0.2, Sarstedt, Germany). The colloids were washed three times by centrifugation at 2700 rcf for 90 seconds, each time replacing the supernatant with conditioned culture medium. After the final wash, the colloids were sonicated for 10 minutes to disrupt any aggregates. TSB is a high-ionic strength medium (≈ 130 mM salt equivalent, pH 7.0–7.2) in which electrostatic interactions are strongly screened (Debye length < 1 nm); the physicochemical environment was identical in suspensions with and without bacteria, ensuring that effective interactions are short-ranged and dominated by steric exclusion. Note that the selected colloid size was chosen to match the sedimentation velocity of *C. denitrificans*, ensuring comparable gravitational Péclet numbers between bacteria and colloids (see Fig. 2b). To this aim, the gravitational Péclet number was estimated as

$Pe_g = V_0(\rho_p - \rho)ga/(k_B T)$, with ρ_p and ρ the density of the particles and the liquid respectively, V_p the volume of a particle, T the temperature, g the gravitational acceleration constant and k_B the Boltzmann constant²⁷. Colloids of the selected diameter have $Pe_g \sim 2.53$, that falls within the range estimated for *C. denitrificans* bacterial cells ($Pe_g = 1.7 - 4.4$), assuming a cell radius of approximately ~ 0.5 μ m, a length within the 3 - 5 μ m range, and a density $\rho_p = 1.0825$ g/cm³.

1.4 Bacteria/Colloid Suspensions

We prepared three types of mixed bacterial-colloidal suspensions, each with a different concentration of colloidal particles (hereafter referred to as 'colloidal densities'). To this end, a bacterial suspension was divided into three 1 mL aliquots and centrifuged at 2700 rcf for 5 minutes to sediment the cells. Subsequently, 100 μ l, 50 μ l or 25 μ l of supernatant was replaced with an equal volume of colloidal suspension, yielding final volumetric colloid-to-bacteria ratios of 1:10, 1:20, and 1:40, respectively. These mixtures correspond to final colloidal densities of 1.68×10^8 particles/mL ('1:10', high density), 8.4×10^7 particles/mL ('1:20', medium density), and 4.2×10^7 particles/mL ('1:40', low density). Each suspension was vortexed for 90 seconds to ensure proper resuspension of the solid phase.

1.5 Bacteria-only and Colloids-only Suspensions

To assess the reciprocal influence between colloids and the bacterial network, we performed two sets of control experiments: one with bacteria-only and one with colloids-only suspensions. In the colloids-only controls, we used the same particle concentrations as in the corresponding mixed suspensions. Each sample was prepared by following the same liquid exchange procedure, starting from 1 mL of conditioned culture medium per mixture (see Fig. 3a, c, e). For the bacteria-only control experiments, we used the same bacterial cultures used as in the mixed suspensions, thereby maintaining identical bacterial concentrations across conditions.

1.6 Microscopy and Imaging Conditions

Imaging was performed in both fluorescence and brightfield modes using an inverted microscope (Nikon Ti, Nikon, Japan). Images were acquired at 20 \times magnification (NA 0.5) with a 1.5 \times zoom (equivalent to a final 30 \times magnification), using sCMOS camera (Photometrics Prime BSI, Teledyne, USA; pixel size 6.5 μ m). Bacteria were imaged in brightfield mode with the condenser aperture set to 50 % closure. Fluorescent imaging was used to visualise the colloidal particles, with excitation at 555 nm and emission at 570 nm (Lumencor Spectra, Lumencor, USA). The depth of focus of the optical configuration at 550 nm was approximately 2.85 μ m, as estimated from the theoretical axial resolution of the imaging system using the standard wave-optical formulation for depth of field ($DOF \approx \lambda n / NA^2$, where λ is the wavelength, n is the refractive index of the immersion medium, and NA is the numerical aperture). This value should be interpreted as an estimate of the axial extent contributing to the image, i.e. an upper bound for the optical section thickness. We



acquired images immediately above the capillary floor, 1.5 μm into the sample. For each field of view, the optimal focus was re-established using the glass surface as a reference, ensuring that the near-wall bacterial layer was consistently imaged within the central, highest-resolution portion of the optical section despite minor local variations across the sample. Since the colloids have a diameter of 3.0 μm and the average bacterial width is approximately 1 μm , one optical section contains at most a single colloid layer and the portions of the bacterial branches that intersect the plane. All samples were imaged 140 minutes after capillary placement on the microscope stage, to ensure complete sedimentation. For each condition, three biological replicates from independent bacterial cultures were prepared to ensure reproducibility. At least four fields of view were acquired per sample to provide statistical robustness.

1.7 Structural characterisation of bacterial network

Characteristic lengths. – The presence of emerging length scales in the bacterial network was evaluated by performing the Fourier analysis of the images of the bacteria-only suspensions acquired by phase-contrast microscopy²⁸. To minimise artefacts caused by sharp image boundaries, we additionally first applied a windowing procedure to the raw 2048 \times 2048 pixels² square images. Specifically, the greyscale intensity at each point (x, y) was multiplied by a two-dimensional circular Tukey window $H(x, y)$ ²⁹.

$$\begin{cases} H(x, y) = 1, & r \leq \alpha L/2 \\ H(x, y) = \frac{1}{2} \left[1 + \cos \frac{\pi(r - \alpha L/2)}{(1 - \alpha)L/2} \right], & \alpha L/2 < r \leq L/2 \\ H(x, y) = 0, & r > L/2 \end{cases} \quad (1)$$

with L the size of the image, $r = \sqrt{(x - L/2)^2 + (y - L/2)^2}$ the radial position of the point (x, y) with respect to the centre of the image and $\alpha = 0.5$ a scaling factor. We then computed the frequency-domain representation of the windowed image by applying a fast Fourier transform (FFT). The resulting

2D power spectrum was integrated over the angular coordinate from 0 to π to obtain a radially averaged profile. Finally, the resulting curves were transformed back from Fourier space to real space to extract the radial profile of the integrated power spectrum, denoted as $\langle I(r) \rangle$. The analysis was performed with an in-house code written in ImageJ-macro language, based on the native ImageJ FFT plugin, the Windowing plugin³⁰ and Radial Profile Extended plugin³¹, combined with an in-house Matlab code. Note that we chose to extract the characteristic mesoscopic length scale using the FFT approach rather than the ‘chord-length’ method proposed by other authors³², as the latter requires binarising the microscopy images and therefore makes the results sensitive to the choice of threshold. Conversely, the FFT can be applied directly to grayscale images and is a well-established methodology in the analysis of isotropic, disordered, network-like structures with a characteristic domain size.

Directionality. – To assess the presence of preferential directions in the pattern, we computed the local orientation of the

image intensity gradient at each point using a Sobel filter (5×5 pixels)³³. The analysis was implemented by means of the ImageJ ‘Directionality’ plugin³⁴.

1.8 Structural characterisation of colloidal patterns

1.8.1 Nearest-neighbours level

We characterised the spatial patterns formed by the colloids in the mixed suspensions and compared them to those in the colloids-only suspensions. To this end, we first extracted the position of the colloidal centroids from the fluorescence images using the TrackMate Fiji plugin³⁵. Based on these positions, we computed various local structural parameters and their corresponding probability distribution functions (PDFs), which are detailed in the following sections.

Coordination number. – The coordination number n_c of a particle is defined as the number of its nearest neighbours. To calculate it, we counted, for each colloid, the number of particles located within a distance $r_n = 2ar_0$ from its centre, where r_0 is the average colloid radius and a is a dimensionless constant. In our analysis, we set $a = 1.25$, and verified that the results remain qualitatively unchanged when a is varied by up to 10%. This choice of r_n and its variation range corresponds to the position of the first minimum in the radial distribution function $g(r)$, which identifies the first nearest-neighbours shell.

Centrosymmetry parameter. – We further evaluated short-range ordering by calculating the centrosymmetry parameter of the colloids, based on their $N = 6$ nearest neighbours, following the method introduced in³⁶:

$$CSP = \sum_{i=1}^{N/2} |\mathbf{r}_i + \mathbf{r}_{i+N/2}|^2 \quad (2)$$

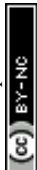
where \mathbf{r}_i and $\mathbf{r}_{i+N/2}$ are vectors from the central particle to two neighbours on opposite sites.

1.8.2 Mid-range level

Mid-range order parameter. – To characterize mid-range ordering, for each particle we calculated the mid-range order parameter s_2^i , defined in^{26,37–39} as the ‘local entropy’ and approximated as the two-body excess entropy^{26,37}. Such a parameter is always negative, with more ordered structures corresponding to lower (i.e. more negative) values. For each particle i , the mid-range order parameter calculated over a neighbourhood of radius r_m is

$$s_2^i = -\pi\rho k_B \int_0^{r_m} [g_m^i(r) \ln g_m^i(r) - g_m^i(r) + 1] r dr \quad (3)$$

where ρ is the particle density, k_B the Boltzmann constant, r the radial coordinate and $g_m^i(r) = \frac{1}{2\pi\rho r} \sum_j \frac{1}{\sqrt{2\pi\sigma^2}} \exp^{-(r-r_{ij})^2/(2\sigma^2)}$ a modified version of the radial distribution function centered around the i^{th} particle, with r_{ij} the distance between particles i and j , and σ a broadening parameter (here $\sigma = 0.05$). To mitigate the effects of fluctuations, we calculated the average local



entropy mid-range order parameter

$$\bar{s}_2^i = \frac{\sum_j s_2^j f(r_{ij}) + s_2^i}{\sum_j f(r_{ij}) + 1} \quad (4)$$

where $f(r_{ij}) = \frac{1-(r_{ij}/r_a)^N}{1-(r_{ij}/r_a)^M}$ is a switching function with a cutoff $r_a = r_m$, $N=6$ and $M=12$. The averaged local entropy mid-range order parameter provides a stronger footprint of local ordering than the non-averaged one^{26,37–39}. Note that the absolute value of \bar{s}_2 depends on the details of the estimation of the radial distribution function in Eq. (3), but its comparative value across different systems is still significant, as long as such details are kept constant⁴⁰. Since the particle positions are extracted from a single near-wall optical section, $g_m^i(r)$ should be understood here as an effective in-plane local pair-correlation function of the imaged layer, rather than as the bulk 3D radial distribution function of the full suspension. We use \bar{s}_2^i for our analysis instead of $g_m^i(r)$ because the latter, though also localized at the particle i , is still a function of distance, whereas \bar{s}_2 provides a single scalar summary of the local correlation profile over the range $0 < r < r_m$. Accordingly, Eq. (3) is not a thermodynamic entropy, but it is as a scalar structural functional of the measured local pair correlation, useful for comparative analysis across samples.

Relative mutual information. – To quantify the relationship between any two properties associated with each colloidal particle, we computed the relative mutual information between them, in line with the approach proposed in⁴¹ for soft matter systems⁴². In particular, we evaluated the relative mutual information $M(N_C, S)/I(N_C)$, between the coordination number and the average mid-range order parameter \bar{s}_2^i calculated at a given length scale r_m . For a given cutoff r_m , the mutual information $M(N_C, S)$ is calculated as²⁴

$$M(N_C, S) = \sum_{n_C, \bar{s}_2} p(n_C, \bar{s}_2) \log \frac{p(n_C, \bar{s}_2)}{p(n_C)p(\bar{s}_2)} \quad (5)$$

where S and N_C are the set of the mid-range order parameters and coordination numbers of the N particles of the system $\{S: \bar{s}_2^i(r_m) \in S, i = 1, \dots, N\}$ and $\{N_C: n_C^i \in N_C, i = 1, \dots, N\}$ respectively; $p(n_C)$ and $p(\bar{s}_2)$ are the probabilities that, for a particle i , the coordination number is $n_C^i = n_C$ and the average mid-range order parameter is $\bar{s}_2^i = \bar{s}_2$, while $p(n_C, \bar{s}_2)$ indicates a joint probability. The self-information of N_C is calculated as

$$I(N_C) = - \sum_{n_C} p(n_C) \log p(n_C). \quad (6)$$

Cluster analysis. – We identified the clusters as ensembles of particles within a distance $r_c = 2ar_0$ from each other. For each cluster, the gyration radius was calculated as $R_g = \sqrt{\sum_{i=1}^s r_i^2}/s$, where r_i is the distance between the i^{th} particle of the cluster and the cluster's centre of mass and s is the cluster's size, namely the number of colloids belonging to the cluster. Furthermore, we assessed the structure of the clusters, as emerging from the juxtaposition of uniform building units - *i.e.* similar local environments - by determining their tiling structure by triangular 'cliques' (*i.e.* triplets of adjacent colloids) and their network topology. To

this aim, we first filtered out singlets and doublets, namely particles with less than two neighbours, by applying a rolling ball search algorithm⁴³ with a radius r_c around each particle. We then created an undirected graph with the (x, y) coordinates of the remaining colloids as nodes. The edges were delimited by pairs of neighbouring colloids, *i.e.* colloids within a distance r_c . The connected components of the graph, detected through the algorithm described in^{25,44}, corresponded to the colloidal clusters. Hence, their tessellation in triangular tiles was retrieved by detecting the completely connected 3-nodes subgraphs, *i.e.* the 3-cycles. Nodes that belonged to such triangular tiles were called 'clique-like' nodes. Nodes that did not belong to such triangular tiles and hence featured two neighbours unconnected to each other, were called 'branch-like nodes'. Then, we evaluated the structural compactness of each cluster through the parameter $a_b = s_b/s$, where s_b is the number of branch-like nodes in the cluster itself. Low values of a_b indicate a more compact cluster structure, hence we refer to a_b as the 'airiness parameter'. Similarly, for the whole system, we evaluated the 'global airiness parameter' $A_b = N_b/N_{tot}$, where N_b and N_{tot} denote the total number of branch-like colloids and the total number of colloids (with the exclusion of singlets and doublets) respectively. A_b indicates the probability that neighbouring nodes are also connected, and it is therefore a measure of graph connectivity. The analysis was performed with an in-house Python code leveraging the NetworkX⁴⁵ package.

1.8.3 Global level

Lacunarity. – The lacunarity λ of the colloidal pattern was calculated based on the detected positions of the colloidal centroids as

$$\lambda = \frac{\langle N(d)^2 \rangle - \langle N(d) \rangle^2}{\langle N(d) \rangle^2} \quad (7)$$

where $N(r)$ is the number of particles inside a square box of size d and $\langle \cdot \rangle$ denotes the average over all particle-containing boxes.

Elastic backbone. – The elastic backbone of the percolating structure was defined as the union of all the shortest paths connecting two representative points, P_1 and P_2 ⁴⁶. The length of each of such paths was denoted as L_b . In order to extract the elastic backbone, we processed the images collected by phase-contrast microscopy as described below. First, we performed a contrast-limited adaptive histogram equalisation (CLAHE)⁴⁷. We then binarised the resulting images via thresholding, and we despeckled them with a median filter based on a 3x3 pixel square. In the resulting black and white images, both bacteria and particles were depicted in white, while the background was black. Such images were skeletonised by applying the thinning algorithm described in⁴⁸. The extracted skeleton underwent an additional dilatation to match the thickness of the bacteria. Hence, we were able to extract the binarised connected bacterial structure. For the mixed suspensions, additional steps were required to guarantee that the colloids incorporated inside the network were correctly represented. To this aim, we separately reconstructed the binarised representation of the colloids, and we subsequently added it to the bacterial network. The binarised representation of the colloids was reconstructed by using the positions of their centroids



as detected by TrackMate³⁵ from the fluorescence images. Using such positions, we constructed a binary mask of single pixels, and we then applied a morphological dilatation filter based on a disk structure matching the colloidal diameter. Hence, we summed this image to the previously extracted binary bacterial network to reconstruct a binarised version of the complete percolating structure. These operations were performed by using an in-house code written in ImageJ macro language based on the FiJi native plugins 'CLAHE', 'Threshold', 'Remove outliers' and 'Skeletonize', as well as the 'Morphological filters' from the MorphoLibJ toolbox⁴⁹. Finally, we used the binarised image representing the percolating structure to extract the elastic backbone by means of the burning algorithm⁴⁶. To this end, in each image we identified the largest connected area and selected its two most distant points, P_1 and P_2 , corresponding as closely as possible to the extremes of one of the image diagonals. The burning algorithm was then applied using P_1 as the starting point and P_2 as the endpoint, employing an 8-connected neighbourhood scheme to identify connected pixels.

A list of the main symbols used throughout the manuscript is provided in Table 1. A sketch of the workflow adopted to characterize the patterns formed by the colloids is displayed in Fig. 1.

Symbol	Description
a_b	airiness parameter of a cluster
A_b	global airiness parameter
CSP	centrosymmetry parameter
k_B	Boltzmann constant
$f(r_{ij})$	switching function used to calculate \bar{s}_2^i
$g(r)$	radial distribution function (2d)
$g_m^i(r)$	modified version of $g(r)$ centered around particle i
$I(N_c)$	self-information of coordination number
$\langle I \rangle$	power spectrum of FFT
L_b	length of elastic backbone between points P_1, P_2
$M(N_c, S)$	mutual information n_c and \bar{s}_2^i
n_c	coordination number
$N(d)$	number of particles inside a square box of size d
N_b	total number of branch-like particles
N_b^*	total number of branch-like clusters
N_c^*	total number of clique-like clusters
N_{tot}	total number of particles
N_{tot}^*	total number of clusters
$P_1 P_2$	distance between points P_1, P_2
r	radial coordinate
r_0	average particle radius
r_c	inter-particle distance in clusters
R_g	cluster gyration radius
r_n	inter-particle search distance used to calculate of n_c
r_a	cutoff of the switching function $f(r_{ij})$
r_i	distance between particle i and cluster's centre of mass
r_{ij}	distance between i^{th} and j^{th} particles
r_m	radius of area around particle i used to calculate \bar{s}_2^i
s	cluster size (particle number)
s_b	number of branch-like nodes in a cluster
\bar{s}_2^i	mid-range order parameter of particle i
\bar{s}_2	average mid-range order parameter
λ	lacunarity
σ	broadening parameter used to calculate $g_m^i(r)$

Table 1 List of main symbols

2 Results and discussion

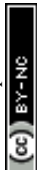
Bacterial network. – After sedimentation, *Comamonas denitrificans* formed a percolating network that spanned the entire field of view, composed of branched, interconnected structures distributed across the capillary floor, consistent with previous observations for *C. denitrificans*⁵⁰ (Fig. 2a). Cells were visualised in a focal plane located 1.5 μm above the capillary floor, within a single optical section of thickness 2.85 μm ; therefore, the observations reported here specifically probe the near-wall bacterial layer. The experiments were performed using stationary-phase cells, for which growth during the experimental time frame was negligible; therefore, the interactions within this network are governed by geometric confinement and the bacterial cell surface properties.

We performed Fourier analysis on bacteria-only suspensions to access the characteristic length scales. Peaks in the power spectrum $\langle I(r) \rangle$ revealed a dominant spatial frequency corresponding to a characteristic length of approximately $7.5 \pm 1 \mu\text{m}$ in the bacterial network (Fig. 2c). Visual inspection confirmed this length matched the width of bacterial branches and the gaps between them (Fig. 2a). Additionally, we investigated the presence of preferential directions by determining the orientation of the local gradient of the image intensity at each point, as detected by Sobel filtering³³. The resulting probability distribution (PDF) of orientations θ indicated no dominant direction (Fig. 2d). We thus conclude that the bacterial network is isotropic.

Mixed bacterial/colloidal suspensions. – In the mixed suspensions, colloids were embedded within the bacterial network. Bacteria altered colloidal clustering, increasing heterogeneity in the resulting clusters (Fig. 3b-e-h) compared to colloids-only suspensions (Fig. 3a-d-g). To quantify this effect, we performed a structural analysis of the colloidal aggregates in the mixed and colloids-only suspensions. Our analysis spanned multiple spatial scales: local (nearest neighbours), mid-range, and global (system-spanning). We used probability distribution functions (PDF) of different structural parameters.

2.1 Short-range ordering

We assessed the short-range ordering around each particle by calculating its coordination number, n_c , which reflects the number of nearest neighbours, and the centrosymmetry parameter, CSP , reflecting the symmetry of the six nearest neighbours (see Materials and Methods 1.8.1)³⁶. Low values of the CSP indicate a higher degree of symmetry at the nearest-neighbours level, which is typical of crystalline and solid-like arrangements. Across each particle concentration, the presence of bacteria did not significantly alter the PDFs of n_c compared to the colloids-only suspensions (Fig. 4a). The values we obtain in our system—where the near-wall layer 2D section of a 3D sample are analysed (see Methods)—are compatible with those reported for fully 3D systems imaged by confocal microscopy, in which many particles display 7–8 neighbours⁵¹. Based on geometrical arguments, this difference is expected, as the number of detected neighbours in 2D and 3D scales approximately with n_{1d}^2 and n_{1d}^3 , respectively, where n_{1d}



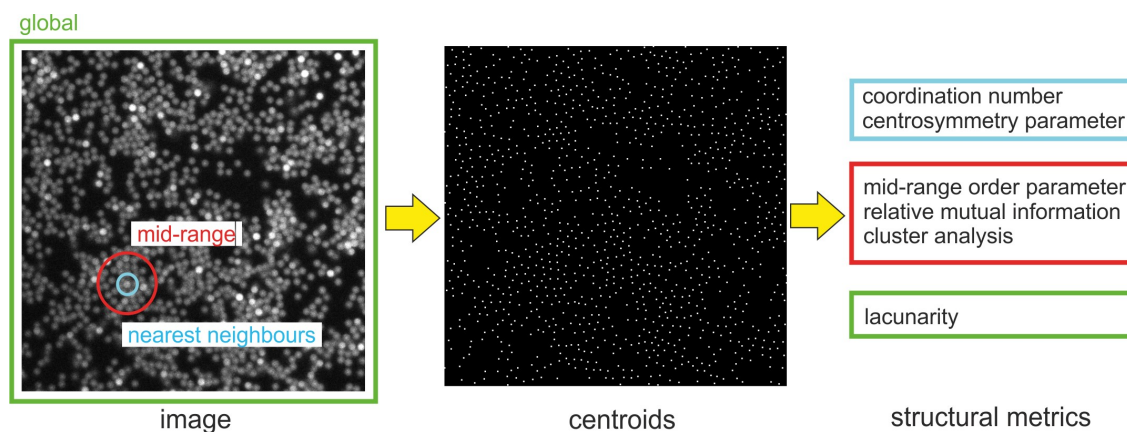


Fig. 1 Sketch of the workflow adopted to characterize the colloidal patterns.

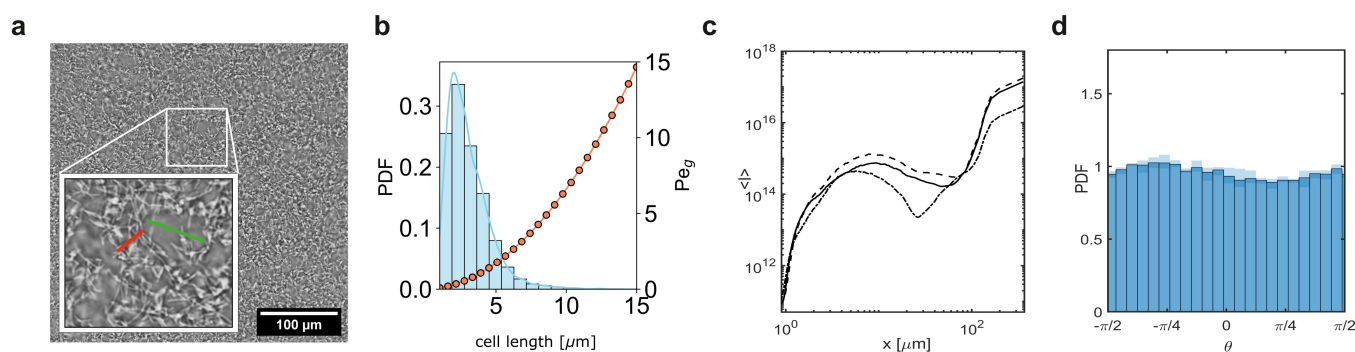


Fig. 2 Characterisation of the isotropic percolating network formed by *Comamonas denitrificans*. (a) Contrast-enhanced phase-contrast microscopy image as observed at the bottom of the cell after 140 min in the bacteria-only suspensions. The red and green lines identify distances of $\sim 7.5 \mu\text{m}$, corresponding to the FFT peaks. They reflect the thicknesses of both branches (red) and empty spaces (green) in the bacterial network, (b) Cell length distribution of the bacterial culture used throughout our experiments and the respective Peclet numbers, (c) Radial profile of the integrated power spectrum $\langle I(r) \rangle$ from the FFT analysis; the three lines represent three biological replicates (d) PDF of the directionality of the image. The shaded area indicates the range spanned over three biological replicates.



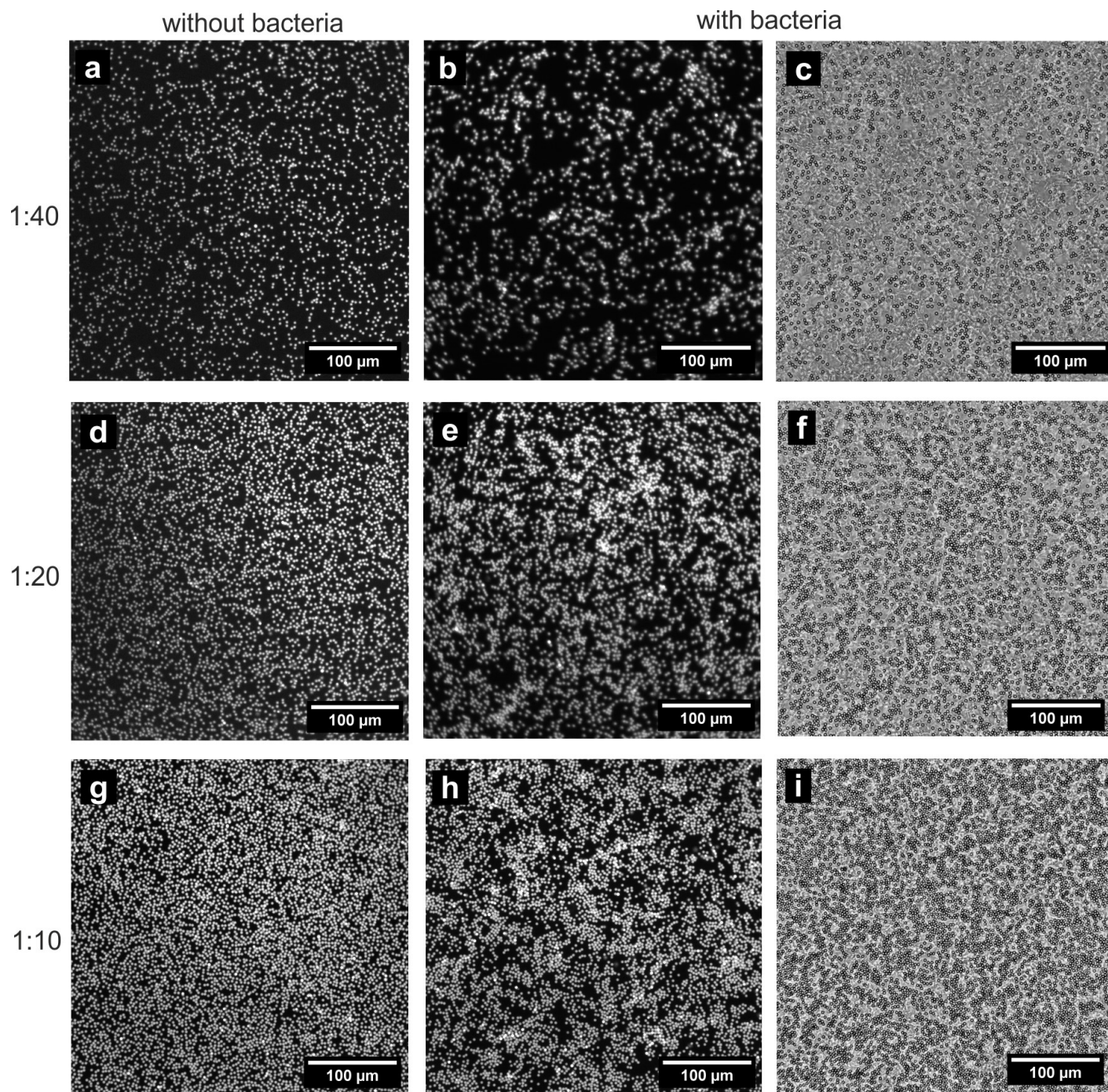


Fig. 3 Patterns at the bottom of the cell after 140 min in the colloids-only suspensions (a,d,g) and in the mixed suspensions (b,c,e,f,h,i) for three colloidal concentrations: (a-c) low, (d-f) medium and (g-i) high. The first two columns, imaged in fluorescence, depict the colloids; the last column, imaged in phase-contrast, depicts both colloids and bacteria. The images are post-processed with contrast enhancement.



denotes the one-dimensional number of neighbours. Similar approaches based on 2D sections of 3D colloidal systems have previously been used to extract structural and dynamical information, provided that all comparisons are performed within a consistent imaging geometry.⁵²

In mixed suspensions, the peaks of the CSP PDFs were shifted towards lower values compared to their colloids-only counterparts, indicating increased local symmetry, consistent with enhanced clustering (Fig. 4b). The shift, however, remained lower than 10 %. Thus, bacteria did not significantly affect nearest-neighbour ordering.

2.2 Mid-range ordering

We characterised mid-range ordering using the average mid-range order parameter \bar{s}_2 , computed for each particle based on the positions of its neighbours within a circular region of radius r_m (see Materials and Methods 1.8.2). Though such a parameter was originally defined in the context of equilibrium systems⁵³, it has subsequently been vastly employed with the name of 'two-body excess entropy' also for non-equilibrium systems^{40,54,55}, including 2D and quasi-2D particle systems^{56,57}. We note, however, that, for such systems, \bar{s}_2 should not be considered as a thermodynamic entropy in the equilibrium sense. Instead, it is a structural metric reflecting ordering on the length-scale r_m that has been proven particularly suitable to identify clustering and nucleated states⁴⁰. We calculated the probability distribution function of \bar{s}_2 using r_m equal to $4ar_0$ and $8ar_0$, corresponding to approximately two and four coordination shells, respectively (Fig. 5a-b).

In each case, the \bar{s}_2 distributions were broader for mixed suspensions than for colloids-only suspensions (insets Fig. 5a-b), indicating increased structural heterogeneity in the presence of bacteria. For mid-range order parameters calculated with a cutoff $r_m = 4ar_0$, the peak of the distribution shifted to the left in mixed suspensions with middle (red curve) and low particle concentrations (yellow curve). This indicates that ordering on the length scale of the second neighbouring shell is more pronounced when bacteria are present. Conversely, for high colloidal concentrations (blue curve), the presence of bacteria did not affect the position of the peak. Interestingly, when the mid-range order parameter were calculated with a cutoff $r_m = 8ar_0$, the situation was reversed: for middle and low particle concentrations, the position of the peak was not influenced by the presence of bacteria, while for high particle concentrations the peak of the mixed suspensions had a shift towards the right with respect to their colloids-only counterpart. This suggests that at high colloidal concentrations, ordering at the scale of the fourth neighbour shell is more pronounced in the absence of bacteria.

Ordering propagation. – To gain further insights into the different behaviour of the the examined systems on different length scales, we investigated how local nearest-neighbours ordering influenced mid-range ordering. We evaluated the relative mutual information $M(N_C, S)/I(N_C)$, between the coordination number and the average mid-range order parameter calculated for a given cutoff distance r_m , where $M(N_C, S)$ denotes the mutual information and $I(N_C)$ the self-information of the coordination number

(Fig. 6). The relative mutual information $M(N_C, S)/I(N_C)$ can be interpreted as a correlation, namely a number between 0 and 1, quantifying how much information one has on the mid-range order parameter of a particle i , if its coordination number n_C^i is known. The higher the relative mutual information, the stronger the correlation. Since \bar{s}_2 quantifies ordering around a particle i over a distance r_m , by varying r_m we could establish the spatial influence of the coordination number (reflecting the nearest-neighbour arrangement) on the ordering degree over a length scale r_m .

The relative mutual information trends were similar for mixed (solid lines) and colloids-only suspensions (dashed lines) for low and middle particle concentrations, but at high particle concentrations, the colloids-only suspension displayed a peak near $7 \mu\text{m}$ (corresponding to 3-4 neighbouring shells), absent in mixed suspensions. The presence of a peak at a given distance r_m^* indicates a stronger interdependence between coordination number and mid-range order parameter at this distance. We interpret r_m^* as a "propagation distance" of mid-range ordering. Conversely, no peak indicates a more heterogeneous, disordered structure. This was confirmed by the observation that, for high particle concentrations, on the length scale of two neighbouring shells ($r_m = 4ar_0$) the PDFs of mid-range order parameters had a peak at the same location regardless the presence of bacteria (Fig. 5a), while on a length scale of four neighbouring shells ($r_m = 8ar_0$) colloids-only suspensions had a lower \bar{s}_2 , *i.e.* a higher ordering degree (Fig. 5b).

We conclude that in colloidal-only suspensions, the local ordering of the nearest neighbours propagates up to 3-4 shells around a particle, whereas for mixed suspensions it stops after the first. We attribute this to the isotropic orientation of the bacterial network. Hence, it acts as a filter by mechanically obstructing the propagation of configurational ordering. Interestingly, the bacterial characteristic length of the bacterial network alone ($\sim 7.5 \pm 1 \mu\text{m}$) was consistent with the suppression of mid-range order propagation beyond 3-4 shells in mixed suspensions.

Cluster analysis. – To investigate how systems that are indistinguishable at the nearest-neighbours level can differ at the mid-range, we analysed the distributions and structure of the colloidal clusters, *i.e.* agglomerates of colloids with an inter-particle distance within $r_m = 2ar_0$. Mixed suspensions at low and medium colloidal densities (red and yellow solid lines) contained more large clusters than their colloids-only counterparts, consistent with the observation that the presence of bacteria promotes colloidal clustering (Fig. 7a, c). However, at high colloidal densities, the differences between the distributions of the colloids-only and mixed suspensions were not significant. Similarly, for all colloidal densities, the maximum cluster size s_{max} and the maximum gyration radius R_g^{max} were not substantially affected by the presence of bacteria (see insets in Fig. 7b, d).

We further analysed the cluster structure by identifying repeating building blocks using a graph theory approach, where colloids are treated as nodes. Nodes with less than two neighbours were excluded. In particular, we investigated the topology of triangular 'cliques' *i.e.* triplets of adjacent colloids. The nodes were clas-



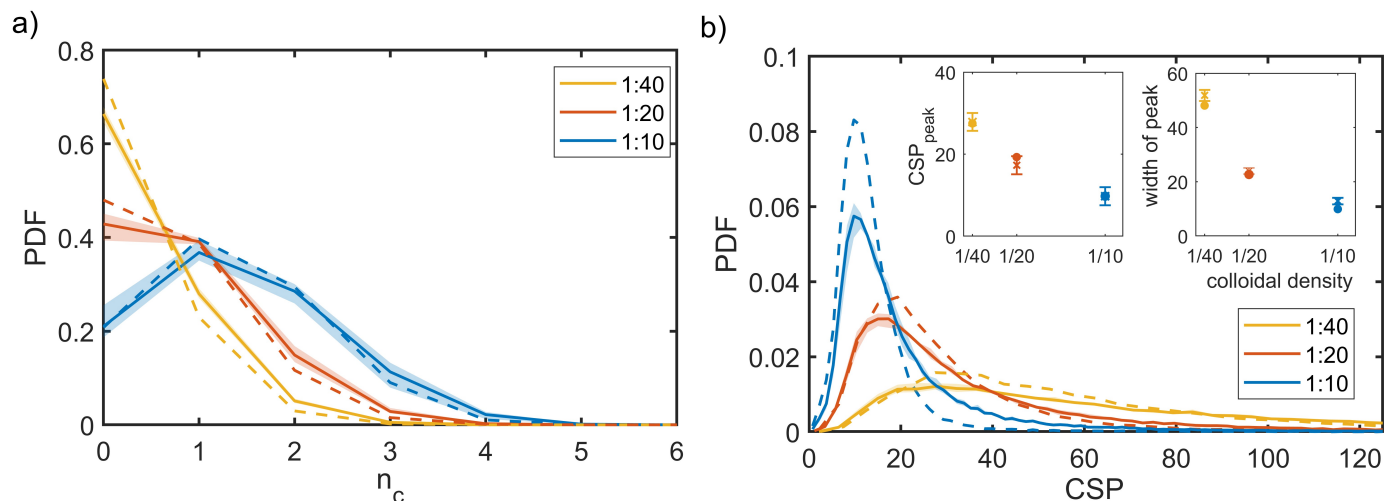


Fig. 4 Characterisation of short-range ordering of colloidal patterns. Probability distribution function of (a) coordination number and (b) centrosymmetry parameter of the colloidal particles in mixed suspensions (solid lines) and in colloids-only suspensions (dashed lines), with high (blue), medium (red), and low (yellow) particle concentrations. The shaded areas represent the biological uncertainty ranges (minimum–maximum across three biological replicates). The insert depicts the location of the peaks without (circles) and with bacteria (crosses), with the error bars reflecting variation within biological replicates.

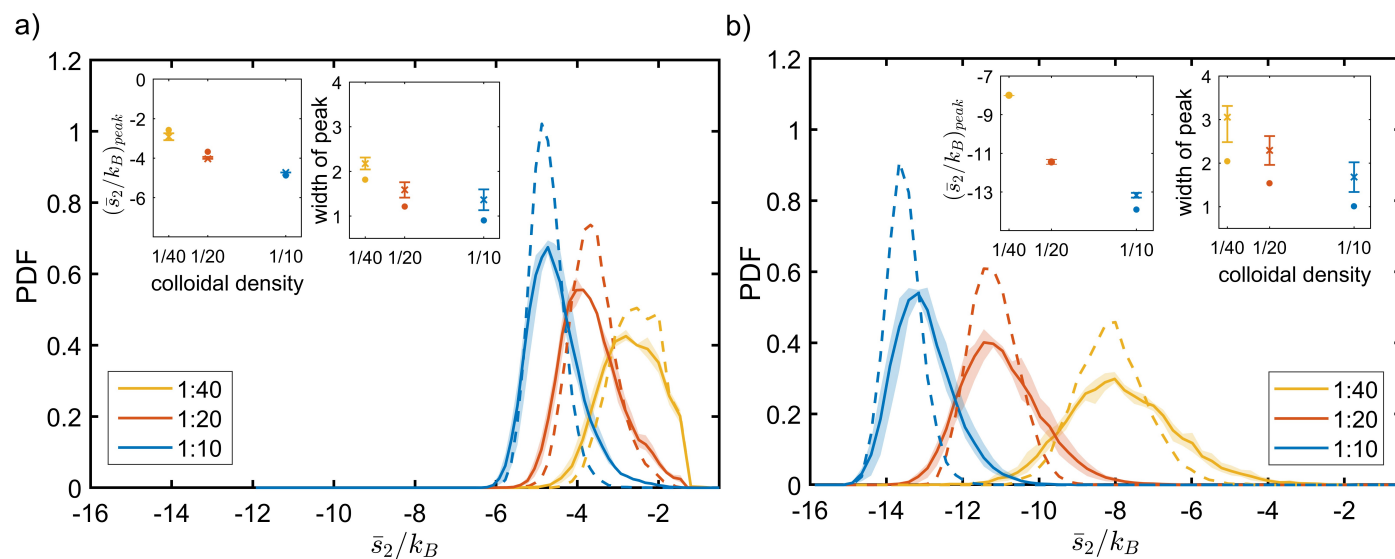
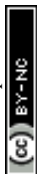


Fig. 5 Analysis of mid-range order parameter of colloidal patterns. Probability distribution function of average mid-range order parameter of colloidal particles calculated with (a) $r_m = 4a_0$ (corresponding to 2 neighbouring shells) and (b) $r_m = 8a_0$ (corresponding to 4 neighbouring shells) for mixed (solid lines) and colloids-only suspensions (dashed lines) for high (blue), medium (red), and low (yellow) particle concentrations. The shaded areas represent the biological uncertainty ranges (minimum–maximum across three biological replicates).



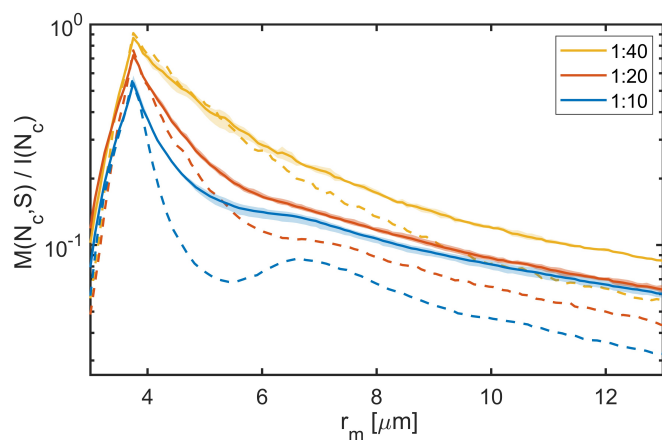


Fig. 6 Relative mutual information between coordination number and average mid-range order parameter at different length scales r_m for suspensions of mixed (solid lines) and colloids-only suspensions (dashed lines) for high (blue), medium (red), and low (yellow) particle concentrations. The shaded areas represent the biological uncertainty ranges (minimum–maximum across three biological replicates).

sified as 'clique-like' (belonging to triangular cliques, compact), or 'branch-like' (non-clique, open). The global airiness parameter $A_b = N_b/N$, where N_b and N are the number of branch-like nodes and the total number of connected nodes, respectively was 40-50% higher in the mixed suspensions, indicating a more open structure (Fig. 7e), consistent with the global lacunarity analysis (see Sect. 2.3). To examine the distribution of branch-like nodes, we distinguished three types of clusters: mixed (clique cores with branches); purely clique-like, and purely branch-like. Their structure was quantified using an airiness parameter $a_b = s_b/s$, where s_b is the number of branch-like nodes in the cluster (Fig. 7.f). The distribution of the airiness parameter showed little difference between systems at low and medium densities, but at high density, the mixed suspensions contained fewer clusters with low a_b . In contrast, purely clique-like and purely branch-like clusters differed between the colloids-only and the mixed suspensions. Bacteria increased the fraction of branch-like clusters N_b^*/N_{tot}^* while decreasing clique-like clusters N_c^*/N_{tot}^* across all densities (Fig. 7g-h). We conclude that differences in global airiness between systems with and without bacteria mainly arise from shifts in the numbers of purely branch-like and purely clique-like clusters, while mixed clusters remain largely unchanged.

2.3 Global ordering

We investigated the patterns formed on a system-spanning scale in the mixed suspensions by considering both the effect of bacteria on the colloidal ensemble and vice-versa. This was done by calculating the lacunarity of the colloidal pattern, as well as by estimating the elastic backbone of the percolation network.

Lacunarity. – We assessed ordering on a global level and the emergence of characteristic length scales by calculating the lacunarity λ of the colloidal pattern, for different system-spanning tessellations with square tiles ('boxes') of side d ⁵⁸. The lacunarity measures the heterogeneity and gappiness of a pattern on the

scale d , with higher λ values indicating a higher heterogeneity on the considered length scale^{59,60}. Mixed suspensions had higher ($\sim 30\%$) and wider ($\sim 30\% - 50\%$) lacunarity peaks, shifted towards larger values of d ($\sim 25\% - 40\%$), compared to colloids-only suspensions (Fig. 8). These changes reflect greater heterogeneity, a broader gap-size distribution, and the presence of larger gaps in the mixed suspensions. This is consistent with the clique analysis, which showed that the bacteria promote a branch-like arier colloidal packing.

Elastic backbone. – Lastly, we evaluated the effect of the colloids on the bacterial network by comparing the percolating structures in bacteria-only and mixed suspensions. We assessed the length of the elastic backbone of the percolating structures, defined as the union of all the shortest paths connecting two representative points P_1 and P_2 ⁴⁶, and we further normalised it by the distance between two such points. The elastic backbone represents the stress-bearing structure of the network⁶¹. Mixed suspensions exhibited longer elastic backbones than bacteria-only suspensions, and backbone length increased with colloidal density (Fig. 9a-c). As the length of the elastic backbone is related to the resistance to stresses, we speculate that the presence of particles reinforces the bacterial network, making it more resistant to disruption.

2.4 Conclusions

In this work, we studied how the presence of sedimenting colloids influences the near-wall layer structure of the percolating network formed by bacteria during sedimentation and how the network, in turn, influences colloidal aggregation. We find that the presence of bacteria favours colloidal clustering. The microscopic origin of the observation was investigated by characterizing the structures emerging in mixed and colloid-only suspensions at different length scales (local, mid-range, global). At the local level, the colloidal arrangement is similar with and without bacteria, as shown by the coordination number and the centrosymmetry parameter. However, at the mid-range scale, we observed enhanced clustering in the presence of bacteria, as evidenced by the increased number of larger clusters in the mixed suspensions. Such clusters were more branch-like and less compact than those in colloids-only suspensions. These observations explain why at the global scale the presence of bacteria induces a greater heterogeneity and gappiness in the colloidal surface-layer pattern, as shown by higher lacunarity values. We attribute this to the randomly orientated bacterial network acting as a barrier to local ordering propagation. This suppression of ordering propagation is not specific to the biological nature of the bacteria, but arises from the presence of a disordered, percolating fibrous scaffold that geometrically constrains colloidal rearrangements. We therefore expect similar behaviour for non-biological rod-like or fibrous networks in the isotropic regime, while different responses may emerge if the scaffold develops orientational (e.g. nematic) order. The conclusion was supported by analysis of the mid-range order parameter local entropy, which quantifies the mid-range ordering. We found that in purely colloidal suspensions ordering was stronger and propagated further (up to 3-4 particle shells) than



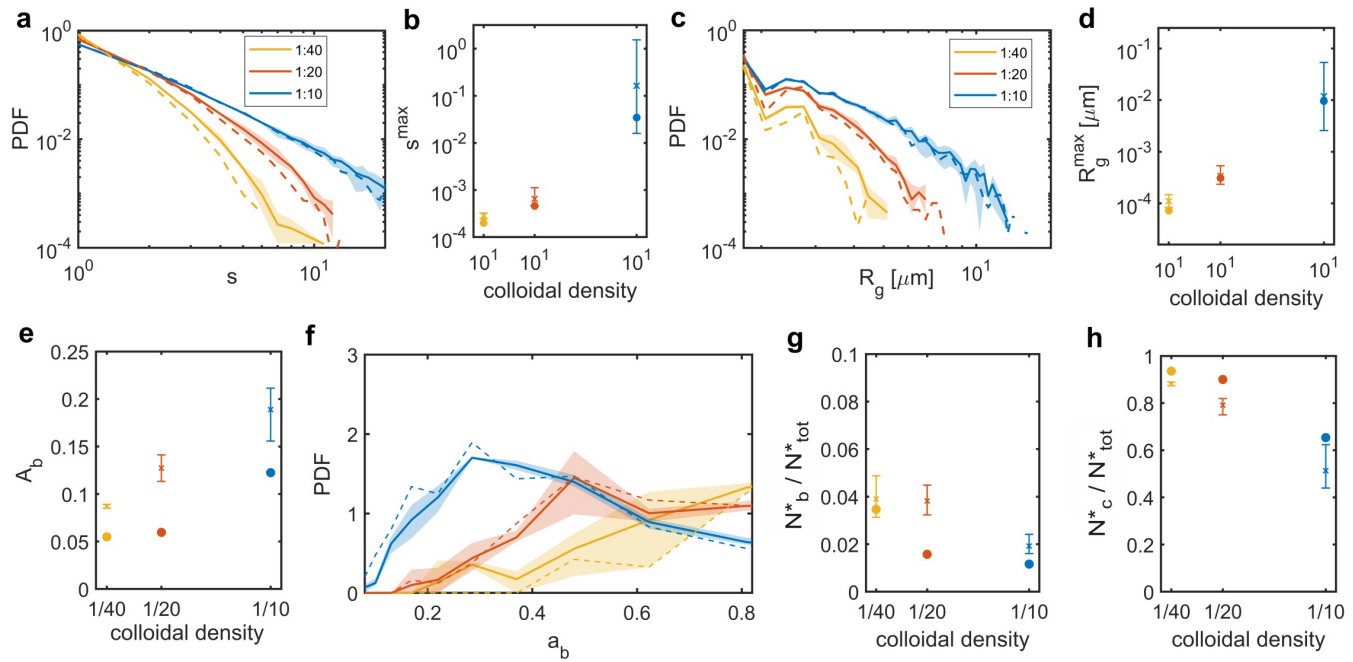


Fig. 7 Cluster distribution and tiling analysis. Probability distribution functions of cluster distributions (a, b) sizes and (c, d) gyration radii of clusters formed by colloids within a distance $r_m = 2ar_0$ from each other for suspensions of mixed (solid lines) and colloids-only suspensions (dashed lines) for high (blue) and medium (red) particle concentrations. (e) Analysis of tiling structures and compactness of the colloidal patterns. Global airiness parameter for colloids only (circles) and mixed suspension (crosses). (f) Probability distribution function of the airiness parameter a_b of the clusters featuring both branch-like and clique-like nodes for mixed (solid lines) and colloids-only suspensions (dashed lines). (g) Ratio of colloids belonging to purely branch-like clusters over the total number of colloids. (h) Ratio of colloids belonging to purely clique-like clusters over the number of colloids. For all figures, the color identifies the different colloidal densities: high (blue), medium (red), and low (yellow). The shaded areas represent the biological uncertainty ranges (minimum–maximum across three biological replicates).



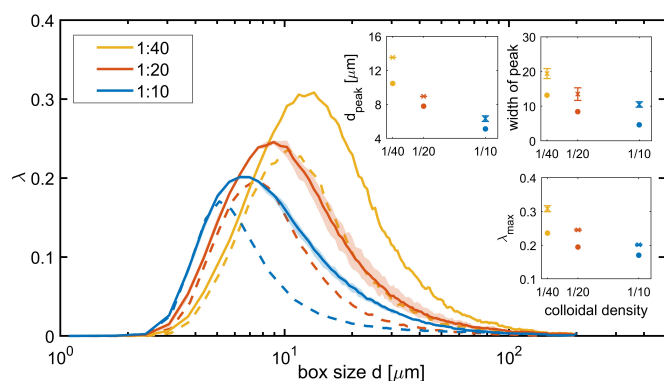


Fig. 8 Global lacunarity of colloidal structure as a function of box size d for mixed suspensions (solid lines) and colloids-only suspensions (dashed lines) for high (blue), medium (red), and low (yellow) particle concentrations. The shaded areas represent the biological uncertainty ranges (minimum–maximum across three biological replicates).

in mixed suspensions.

Finally, we assessed the effect of the colloids on the bacterial near-wall layer network by comparing mixed colloids-bacteria suspensions to the bacteria-only suspensions. In particular, we evaluated the length of the elastic backbone, the load-bearing structure of a percolating system. We found that the presence of colloids resulted in longer elastic backbones, possibly indicating a structure with greater stress resistance, than in the bacteria-only case. Further investigation is needed to confirm this hypothesis, e.g. by evaluating the rheological properties of such suspensions.

While previous efforts to investigate and control near-wall colloidal patterning have typically relied on synthetic depletants or engineered surface geometries, our study is the first to demonstrate that living biological matter can act as a self-assembling scaffold to drive these near-wall microstructural transitions^{62,63}. Overall, our work reveals that the presence of sedimenting non-motile bacteria with colloidal particles gives rise to collective structures distinct from those in purely colloidal and purely bacterial suspensions. These findings provide a basis for using bacterial scaffolds to modulate colloidal assembly and offer a framework for studying particle–network interactions across scales. While primarily fundamental, this approach may also help to rationalise unwanted bacterial aggregation in environmental systems, including those influenced by microplastic contaminants.

Author Contributions

LS and ES developed the original idea. SC, ES and LS designed the experiments. SC and LS performed the experiments. LS and SC performed the data analysis. LS wrote the first draft of the manuscript, and all authors contributed to subsequent versions.

Conflicts of interest

There are no conflicts to declare.

Data availability

The centroid position data used in this study are provided as Supplementary Material in the form of two .xyz files corresponding to high-density suspensions with and without bacteria, which allow

reproduction of the structural analyses shown in Figs. 3–8. All codes used for the analysis are available from the authors upon reasonable request.

Acknowledgements

The authors acknowledge financial support from SNSF PRIMA Grant No. 179834 (to E.S.), MSCA individual fellowship Grant No. 10.3030/101033169 (to S.C.).

Notes and references

- 1 A. Mandal, A. Dutta, R. Das and J. Mukherjee, *Marine Pollution Bulletin*, 2021, **170**, 112626.
- 2 L. Krause, D. Biesgen, A. Treder, S. A. Schweizer, E. Klumpp, C. Knief and N. Siebers, *Geoderma*, 2019, **351**, 250–260.
- 3 L. Zhang, D. Tu, X. Li, W. Lu and J. Li, *BMC Microbiology*, 2020, 254.
- 4 A. Roberto, J. Van Gray and L. Leff, *Water Research*, 2018, **134**, 353–369.
- 5 C. Valeriani, M. Li, J. Novosel, J. Arlt and D. Marenduzzo, *Soft Matter*, 2011, **7**, 5228–5238.
- 6 J. Singh, A. E. Patteson, B. O. Torres Maldonado, P. K. Purohit and P. E. Arratia, *Soft Matter*, 2021, **17**, 4151–4160.
- 7 B. O. Torres Maldonado, R. Ran, K. L. Galloway, Q. Brosseau, S. Pradeep and P. E. Arratia, *Physics of Fluids*, 2022, **34**, 113305.
- 8 T. Yao, v. Kos, Q. Zhang, Y. Luo, E. Steager, M. Ravnik and K. Stebe, *Science advances*, 2022, **8**, eabn8176.
- 9 S. Kamdar, S. Shin, P. Leishangthem, L. Francis, X. Xu and X. Cheng, *Nature*, 2022, **603**, 819–823.
- 10 L. Vaccari, M. Molaei, T. H. Niepa, D. Lee, R. L. Leheny and K. J. Stebe, *Advances in Colloid and Interface Science*, 2017, **247**, 561–572.
- 11 H. Firoozmand and D. Rousseau, *Food Hydrocolloids*, 2014, **42**, 204–214.
- 12 H. Firoozmand and D. Rousseau, *Food Research International*, 2016, **81**, 66–73.
- 13 S. Charlton, G. Melaugh, D. Marenduzzo, C. MacPhee and E. Secchi, *Phys. Rev. E*, 2025, **111**, 024410.
- 14 M. Bantawa, B. Keshavarz, M. Geri, B. Mehdi, D. Thibaut, G. H. McKinley and E. Del Gado, *Nat. Phys.*, 2023, **19**, 1178–1184.
- 15 M. Nabizadeha, F. Nasirianb, X. Li, Y. Saraswatd, R. Waheibid, L. C. Hsiaod, D. Bi, B. Ravandi and S. Jamali, *Proc. Natl. Acad. Sci. U.S.A.*, 2024, **121**, e2316394121.
- 16 G. Tarjus, S. Kivelson, Z. Nussinov and P. Viot, *J. Phys.: Condens. Matter*, 2005, **17**, R1143–R1182.
- 17 C. P. Royall, S. R. Williams, T. Ohtsuka and H. Tanaka, *Nat. Mater.*, 2008, **7**, 556–561.
- 18 B. de Nijs, S. Dussi, F. Smalenburg, J. Meeldijk, D. Groenendijk, L. Fillion, A. Imhof, A. van Blaaderen and M. Dijkstra, *Nat. Mater.*, 2015, **14**, 56–60.
- 19 D. Frenkel, 1999, **263**, 26–38.
- 20 O. Velev, A. Lenhoff and E. Kaler, *Science*, 2000, **287**, 2240–2243.



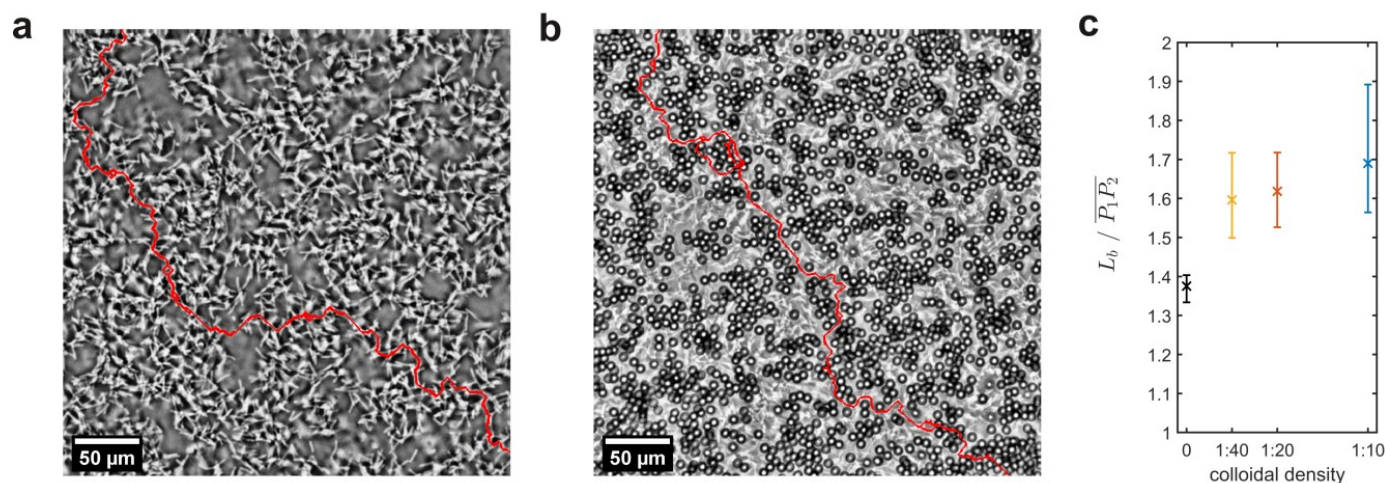


Fig. 9 Analysis of elastic backbone. Examples of elastic backbone (red line) as detected from phase-contrast images (a) in the bacteria-only and (b) in the mixed suspensions; (c) length of the elastic backbone, *i.e.* the shortest path connecting two points P_1 and P_2 as close as possible to the image diagonal normalized by the linear distance separating them $P_1 P_2$, for different colloidal densities: high (blue), medium (red) and low (yellow), compared to the bacteria-only suspension (black). Plotted are the mean and standard deviation from three biological replicates.

- 21 V. Manoharan, M. Elseser and D. Pine, *Science*, 2003, **301**, 483–487.
- 22 F. Bai, D. Wang, Z. Huo, W. Chen, L. Liu, X. Liang, C. Chen, X. Wang, Q. Peng and Y. Li, *Angew. Chem.*, 2007, **46**, 6650–6653.
- 23 S. Wintzheimer, T. Granath, M. Oppmann, T. Kister, T. Thai, T. Kraus, N. Vogel and K. Mandel, *ACS Nano*, 2018, **12**, 5093–5120.
- 24 T. Cover and J. Thomas, *Elements of information theory*, John Wiley & Sons, New Jersey, 2005.
- 25 C. Bron and J. Kerbosch, *Commun. ACM*, 1973, **16**, 575–577.
- 26 J. E. Hallet, F. Turci and P. C. Royall, *Nat. Comm.*, 2018, **9**, 1–10.
- 27 A. E. González, *J. Phys.: Condens. Matter*, 2002, **14**, 2335–2345.
- 28 L. J. Teece, M. A. Faersb and P. Bartlett, *Soft Matter*, 2011, **7**, 1341–1351.
- 29 W. K. Pratt, *Digital Image Processing: PIKS Scientific Inside*, John Wiley & Sons Inc, New York, 2007.
- 30 B. H. Glünder, https://www.gluender.de/Miscellaneous/MiscTexts/MiscExcerpts/ReadMe_W.html, 2020.
- 31 P. Carl, <http://questpharma.u-strasbg.fr/html/radial-profile-ext.html>, 2020.
- 32 L. Testard, V. Berthier and K. Walter, *Phys. Rev. Lett.*, 2011, **106**, 125702.
- 33 R. C. Gonzalez and R. E. Woods, 2014, 186–188.
- 34 J.-Y. Tinevez, G. Cardone, S. J., E. J. and M. Hiner, <https://imagej.net/plugins/directionality>, 2018.
- 35 J.-Y. Tinevez, N. Perry, J. Schindelin, G. Hoopes, G. Reynolds, E. Laplantine, S. Bednarek, S. Shorte and K. Eliceiri, *Methods*, 2017, **115**, 80–90.
- 36 C. K. Kelchner, S. J. Plimpton and J. C. Hamilton, *Phys. Rev. B*, 1998, **58**, 11085–11088.
- 37 P. M. Piaggi and M. Parrinello, *J. Chem. Phys.*, 2017, **147**, 114112.
- 38 H. Tanaka, T. Kawasaki, H. Shintani and K. Watanabe, *Nat. Mater.*, 2010, **9**, 324–331.
- 39 M. Leocmach, J. Russo and H. Tanaka, *J. Chem. Phys.*, 2013, **138**, 12A536.
- 40 P. Piaggi, O. Valsson and M. Parrinello, *Phys. Rev. Lett.*, 2017, **119**, 015701.
- 41 R. L. Jack, A. J. Dunleavy and C. P. Royall, *Phys. Rev. Lett.*, 2014, **113**, 095703.
- 42 E. Stanifer and M. L. Manning, *Soft Matt.*, 2022, **12**, 2394–2406.
- 43 S. R. Sternberg, *Computer*, 1983, **16**, 22–34.
- 44 E. Tomita, A. Tanaka and H. Takahashi, *Theor. Comput. Sci.*, 2006, **363**, 28–42.
- 45 A. A. Hagberg, D. A. Schult and P. J. Swart, Proceedings of the 7th Python in Science Conference, Pasadena, CA USA, 2008, pp. 11 – 15.
- 46 H. J. Hermann, D. C. Hong and H. E. Stanley, *J. Phys. A Math. Gen.*, 1984, **17**, L261–L266.
- 47 K. Zuiderveld, *Graphics gems IV*, Academic Press Professional, San Diego, 1994, pp. 474–485.
- 48 T. Y. Zhang and C. Y. Suen, *Commun. ACM*, 1984, **27**, 235–239.
- 49 D. Legland, I. Arganda-Carreras and P. Andrey, *Bioinformatics*, 2016, **32**, 3532–3534.
- 50 S. Charlton1, G. Melaugh, D. Marenduzzo, C. MacPhee and E. Secchi, *Phys. Rev. E*, 2025, **024410**, 024410.
- 51 W. C. K. Poon, *J. Phys.: Condens. Matter*, 2002, **14**, 7581–7597.
- 52 W. K. Kegel and A. van Blaaderen, *Science*, 2000, **287**, 290–293.
- 53 J. C. Dyre, *J. Chem. Phys.*, 2018, **149**, 210901.



- 54 T. S. Ingebrigtsen and H. Tanaka, *Proc. Natl. Acad. Sci. USA*, 2018, **115**, 87–92.
- 55 S. A. Ghaffarizadeh and G. J. Wang, *J. Phys. Chem. Lett.*, 2022, **13**, 4949–4954.
- 56 Z. Wang, W. Qi, Y. Peng, A. M. Alsayed, Y. Chen, P. Tong and Y. Han, *J. Chem. Phys.*, 2011, **134**, 034506.
- 57 X. Ma, J. Liu, Y. Zhang, P. Habdas and A. G. Yodh, *J. Chem. Phys.*, 2019, **150**, 144907.
- 58 A. Aliche, L. Stricker and J. Vermant, *J. Colloid Interface Sci.*, 2023, **652**, 317–328.
- 59 P. Meakin, *Fractals, scaling and growth far from equilibrium*, Cambridge University Press, Cambridge, 2017.
- 60 T. Smith, G. Lange and W. Marks, *J. Neurosci. Methods*, 1996, **69**, 123–136.
- 61 C. I. N. Sampaio Filho, J. S. J. Andrade, H. J. Hermann and A. A. Moreira, *Phys. Rev. Lett.*, 2018, **20**, 175701.
- 62 N. Nakamura, Y. Sakamoto and H. Ogi, *Scientific Reports*, 2021, **11**, year.
- 63 B. Sprinkle, S. Wilken, S. Karapetyan, M. Tanaka, Z. Chen, J. R. Cruise, B. Delmotte, M. M. Driscoll, P. Chaikin and A. Donev, *Phys. Rev. Fluids*, 2021, **6**, 034202.



Data availability

The centroid position data used in this study are provided as Supplementary Material in the form of two .xyz files corresponding to high-density suspensions with and without bacteria, which allow reproduction of the structural analyses shown in Figs. 3–8. All codes used for the analysis are available from the authors upon reasonable request.

